Article

Development of 180 kW Organic Rankine Cycle (ORC) with a High-Efficiency Two-Stage Axial Turbine

Jung-Bo Sim [1,2], **Se-Jin Yook** [2] and **Young Won Kim** [1,*]

1   Green Energy & Nano Technology R&D Group, Korea Institute of Industrial Technology, Gwangju 61012, Republic of Korea
2   School of Mechanical Engineering, Hanyang University, Seoul 04763, Republic of Korea
*   Correspondence: ywkim@kitech.re.kr; Tel.: +82-062-600-6440

Abstract: The design of turbines used to convert thermal energy into electrical energy in an organic Rankine cycle (ORC) is crucial. A high-speed turbine requires high-performance bearings, which increases turbine manufacturing costs. In this study, a high-efficiency two-stage axial turbine at a low rotational speed was developed, and the ORC performance was presented. We designed a 180-kW axial turbine of 12,000 rpm. To increase turbine efficiency, the number of turbine stages was set to two, and turbine blades were designed to reduce pressure losses. One-dimensional design parameters of blades that minimized the total pressure loss were selected using an in-house code based on a generalized reduced gradient (GRG) nonlinear algorithm. Three-dimensional turbine blade modeling and numerical analysis were performed using commercial software. The total-to-static isentropic efficiency and output of the two-stage axial turbine were predicted to be 85.1% and 176 kW, respectively. ORC performance was assessed using the predicted turbine performance results. Assuming the temperature of the condenser outlet working fluid to be 25 °C, the ORC thermal efficiency and exergy efficiency were found to be 7.40% and 34.49%, respectively. Our findings highlight the applicability of various rotational speeds and number of stages for an axial turbine in an ORC.

Keywords: organic Rankine cycle (ORC); axial-flow turbine; mean-line design; off-design; R245fa

1. Introduction

The use of fossil fuels causes the emission of air pollutants, including greenhouse gases, resulting in environmental issues such as global warming and ozone depletion. To address these issues, research is actively being conducted worldwide on the development of renewable energy that can replace fossil fuels. To convert thermal renewable energy, such as solar heat, geothermal heat, and chemical reaction heat into electricity, a thermodynamic power generation system is required. In the last few decades, the Brayton cycle and the Rankine cycle have mostly been used to produce electricity using thermal energy [1]. In general, the Brayton cycle uses a gas turbine, and the Rankine cycle uses steam to generate electricity. As the organic Rankine cycle (ORC) uses an organic refrigerant as the working fluid, it can produce electricity using a low-grade temperature heat source at 150 °C or less [2].

ORC emits no pollutants while producing electricity and is eco-friendly, as it uses an organic refrigerant with low global warming potential as the working fluid. ORC has been mainly used in factories and in solar heat, geothermal heat, and biomass industries [3,4], and its application range can be gradually expanded, as it can recover low-temperature heat sources. ORC is an economical power generation system that can continuously produce electricity using the pump power consumption alone if evaporation and condensation conditions are satisfied. Various studies have been conducted to improve the efficiency of the ORC under a constant-heat-source condition to generate more electricity.

The working conditions and the organic refrigerant used as the working fluid are representative factors affecting the ORC efficiency. Thus, numerous studies have already been focused on these factors. There are, however, few studies on the performance of the turbine in the ORC system. In the ORC, the turbine plays an essential role in converting the heat recovered from a heat source into mechanical energy. Furthermore, the electrical power output obtained through the turbine and generator directly affects the thermal efficiency of the ORC. Therefore, the design of the turbine is crucial.

Li et al. [5] designed and built a low-temperature geothermal regenerative ORC system with R123. As the mass flow rate was increased, both the turbine inlet pressure and turbine rotation speed increased, whereas the regenerator efficiency exhibited the opposite trend. The turbine power and isentropic efficiency were 6.07 kW and 58.53%, respectively, and the efficiency of the regenerative ORC was 7.98%, which was higher than that of the basic ORC by approximately 1.83%.

Peng et al. [6] investigated the performance of a kilowatt-class axial-flow turbine and proposed a method for improving the turbine efficiency. The preliminary design of the axial-flow turbine was performed for parameter optimization, and the effect of the tip clearance and trailing edge thickness on the turbine performance was analyzed. Consequently, the turbine efficiency could be improved significantly by reducing the tip clearance and trailing edge thickness. When the clearance and trailing edge reached 0.1 mm, the expected efficiency of the two-stage turbine was 82%, which was 33% higher than that of the conventional type.

Fu et al. [7] designed and built a 250 kW ORC system that included a pump, preheaters, evaporators, turbines, generators, condensers, and cooling water circulation systems. Refrigerant R245fa was used as the working fluid, and the maximum net power and system thermal efficiency were 225 kW and 7.94%, respectively. Under this condition, the isentropic efficiency of the turbine was 63.7% at a rotation speed of 12,386 rpm. Moreover, experimental results showed that the system thermal efficiency and net power increased linearly with increasing heat source temperature.

Pei et al. [8] illustrated a newly constructed kilowatt-scale ORC system with R123, which adopted an innovative radial turbine. When the temperature difference between the hot and cold sources was approximately 70 °C, the experimental results showed a turbine isentropic efficiency and ORC thermal efficiency of 65% and 6.8%, respectively. In addition, the turbine demonstrated adequate performance under off-design conditions, indicating that it could be applied for small-scale ORCs.

Kang [9] developed an ORC capable of generating power using a low-temperature heat source. R245fa was used as the working fluid, and a radial turbine coupled with a high-speed generator was designed by considering the cycle conditions. In addition, the efficiencies of the turbine and ORC and the power output of the ORC with respect to its operating conditions were investigated experimentally. As a result, the maximum average cycle, turbine efficiency, and power output were 5.22%, 78.7%, and 32.7 kW, respectively. Further, Klonowicz et al. [10] presented a numerical analysis and preliminary experimental results of a small-scale turbine with the corresponding design assumption and process, and R227ea was used as the working fluid. At a rotation speed of 3264 rpm, the efficiency and electrical power of the turbine were $53 \pm 2\%$ and $9.9 \pm 0.2\%$, respectively.

Giovannelli et al. [11] designed a two-stage radial inflow turbine for small-scale (<100 kW) ORC. The design process included a one-dimensional (1D)/two-dimensional (2D) model and a three-dimensional (3D) computational fluid dynamics (CFD) model. After the preliminary design, sensitivity analysis was performed by varying the relevant geometric parameters to improve the design performance. Thereafter, the performance maps of the two-stages were analyzed under off-design conditions. The efficiency of the two-stages was approximately 80%, and the turbine power at the nominal point (total expansion ratio 3.9) was 71.2 kW. Li et al. [12] presented results of an experimental study performed on a prototype of an axial-flow turbine applied to an ORC system using R123 as the working fluid. In the experiment, the turbine was tested under various conditions (inlet

pressure: 0.6–1.5 MPa, inlet temperature: 80–150 °C, and rotation speed: 3010 rpm). The isentropic efficiency of the turbine could reach 53% at an expansion ratio of approximately 11.0, and the maximum power generated by the turbine generator was 6.57 kW.

Jubori et al. [13] modeled a small-scale two-stage axial turbine and compared it with a single-stage axial turbine to improve the ORC performance. To design the turbine, the preliminary mean-line design approach was coupled with a 3D design, and numerical analysis was performed. In addition, the effect of the turbine on the ORC cycle performance was evaluated. They obtained an isotropic efficiency of the two-stage axial turbine of 83.94%, a power output of 16.037 kW, and an ORC thermal efficiency of 14.19%, compared with 78.30%, 11.06 kW, and 10.5%, respectively, obtained from a single-stage axial turbine with n-pentane as the working fluid.

Jubori et al. [14] explored the turbine design features to maximize the performance of the ORC. For this purpose, in ORC modeling, mean-line design and 3D numerical analysis were integrated for both micro-axial and radial turbines. Both configurations of the turbine were designed in a mass flow rate range of 0.1–0.5 kg/s for five organic fluids (R141b, R1234yf, R245fa, n-butane, and n-pentane). When n-pentane was used as the working fluid, the maximum total-to-total efficiency and power output of the radial turbine were 83.85% and 8.893 kW, respectively, and those of the axial turbine were 83.48% and 8.507 kW, respectively. In addition, the ORC thermal efficiencies were approximately 10.60% and 10.14% with radial and axial turbines, respectively.

Table 1 summarizes the characteristics (type, number of stages, rotational speed, efficiency, and power output) of the aforementioned turbines and ORC thermal efficiency. In particular, in the case of a single-stage axial turbines of 200 kW or less, high rotational speed (>40,000 rpm) was applied to increase the efficiency [6,14–16]. However, a high-rotational-speed turbine requires high-performance bearings such as frictionless bearings.

Table 1. List of recent studies on the characteristics of turbines applied to the ORC.

Authors	Turbine				ORC η [%]	[Ref.]
	Type (Stage No.)	Ω [rpm]	η [%]	$\dot{W}$ [kW]		
Li et al.	Axial (1)	1600–3600	58.53	6.07	6.15–7.98	[5]
Peng et al.	Axial (1–3)	150,000–190,000	75.8–81.6	18.34–19.0	-	[6]
Fu et al.	Axial (1)	12,386	63.7	219.5 ± 5.5	7.94	[7]
Pei et al.	Radial (1)	20,000–25,000	65	1.36	6.8	[8]
Kang	Radial (1)	20,000	78.7	32.7	5.22	[9]
Klonowicz et al.	Axial (1)	3264	53 ± 2	9.9 ± 0.2	-	[10]
Giovannelli et al.	Radial (2)	23,000–27,000	80	71.2	-	[11]
Li et al.	Axial (1)	3010	53	6.57	-	[12]
Jubori et al.	Axial (2)	30,000	78.30–83.94	11.06–16.04	10.5–14.19	[13]

Bearings are one of the important components of a turbine system, which provide the rotation of the turbine rotor. It can also affect turbine performance and turbine system cost [17]. Bearings applied to turbine systems include ball bearings [18], rolling bearings [19], hydrodynamic bearings [20], gas bearings [21,22], magnetic bearings [23,24], etc. Under the high rotational speed of the turbine, the ball bearing technology is not practically realizable because a considerable portion of the energy is lost due to friction [22,23]. Therefore, frictionless bearings such as gas bearings and magnetic bearings are required for high rotational speed conditions, and the turbine system manufacturing cost is high. The use of ball bearings can reduce the cost; however, it lowers the turbine efficiency owing to the low rotational speed. To address this trade-off, in the present study, a two-stage axial turbine with high efficiency even at a low rotational speed (12,000 rpm) was developed. In the developed turbine, ball bearings can be used. To design the high-efficiency turbine blade, a turbine blade that minimized the pressure loss was designed first using the 1D mean-line method. Based on the mean-line design results, a 3D blade geometry was designed, and

numerical analysis was performed using commercial software packages. Furthermore, the turbine performance under off-design conditions was analyzed using the numerical analysis results, and the thermodynamic performance of the ORC with the designed turbine was predicted.

2. Organic Rankine Cycle

2.1. Thermodynamic Description of the Rankine Cycle

The ORC consists of an evaporator, a condenser, a pump, and a turbine system, which are arranged as shown in Figure 1. The evaporator vaporizes the working fluid through heat exchange between the heat source and working fluid. The steam that passes through the evaporator enters the turbine system and produces electricity by converting the thermal energy of the working fluid into mechanical energy. The turbine system generally consists of a turbine, a generator, and a shaft system. The turbine and the generator include multiple stators and rotors. The shaft system comprises a shaft that is supported by a bearing. The conventional structure and flow path of the turbine system are described in detail in a previous study [25]. The condenser condenses the steam that passes through the turbine into a liquid state again, and the working fluid is circulated by the pump. Points 1–4 in Figures 1 and 2 represent the positions in the ORC layout.

Figure 2 shows a typical temperature–entropy diagram that represents the state of the working fluid in the ORC. The region from point 1 to point 2 undergoes the isobaric heat addition process in the evaporator where the working fluid reaches superheated vapor. In the region from point 2 to point 3, the temperature and pressure of the working fluid decrease because of the adiabatic expansion of the turbine. The region from point 3 to point 4 undergoes the isobaric heat rejection process in the condenser where the working fluid reaches saturated liquid. Finally, the region from point 4 to point 1 undergoes the adiabatic compression process where the pressure of the working fluid is increased by the pump. And, the point 1s and 3s represent the phase changes of the isentropic state. Therefore, ORC is a thermodynamic cycle that includes the phase change of the working fluid, and the isobaric and adiabatic processes are repeatedly performed.
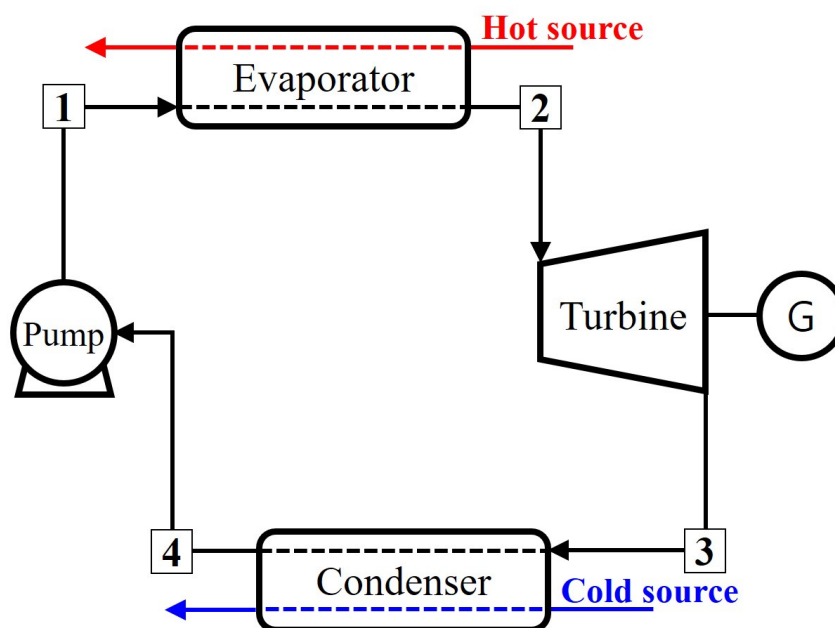

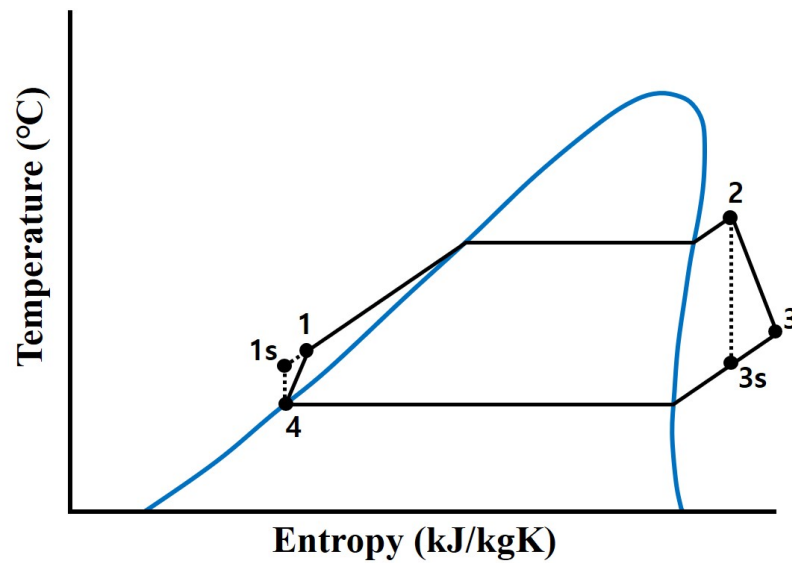**Figure 1.** Schematic diagram of the basic ORC.

Figure 2. Description of the T-s diagram in the ORC.

Table 2 shows the working condition parameters of the ORC system design. The target output of the ORC system is 180 kW. In this instance, the turbine inlet temperature and pressure are 85 °C and 0.75 MP, respectively. The turbine inlet temperature is determined considering the heat exchange from a low-temperature geothermal heat source of approximately 100 °C [26,27]. In addition, the cold source temperature for condensation is assumed to be the ambient temperature (20 °C) of water. The pump and generator efficiencies are assumed to be 75% and 98%, respectively.

Table 2. Working condition parameters of the 180 kW ORC system.

Parameters	Value
Working fluid	R245fa
Inlet temperature, Tin [°C]	85
Inlet total pressure, Pin [MPa]	0.75
Power output [kW]	180
Evaporator & Condenser	Heat exchanger
Pump efficiency, η_p	0.75
Turbine type	Axial-flow
Number of turbine stage	2
Turbine rotational speed [RPM]	12,000
Generator efficiency	0.98
Hot source temperature, T_H [°C]	100
Cold source temperature, T_C [°C]	20

2.2. Mathematical Formulation

The turbine includes irreversibility in the adiabatic process. It has isentropic efficiency, which is defined as the ratio of real Δh to isentropic Δh. the turbine total-to-static efficiency (η_t) and turbine work output ($\dot{W}_t$) are calculated as follows:

$$\dot{W}_t = \dot{m}(\Delta h_0) \tag{1}$$

$$\eta_t = \frac{(\Delta h)_{real}}{(\Delta h)_{isentropic}} = \frac{\Delta h_0}{h_{02} - h_{3s}} \tag{2}$$

Here, the subscript 0 means enthalpy based on total pressure, $\dot{m}$ is mass flow rate, and h_{3s} is the enthalpy based on the static pressure of the turbine outlet in the isentropic process.

The thermal efficiency of the ORC (η_{th}) is defined as the ratio of the network output of the ORC system ($\dot{W}_{net}$) to the heat input from the evaporator ($\dot{Q}_e$), and is calculated as follows:

$$\eta_{th} = \frac{\dot{W}_{net}}{\dot{Q}_e} \tag{3}$$

The exergy efficiency of the ORC, η_{ex}, is defined as the ratio of η_{th} to the Carnot cycle efficiency, η_{car}, and is calculated as follows:

$$\eta_{ex} = \frac{\eta_{th}}{\eta_{car}} \tag{4}$$

$$\eta_{car} = \frac{T_H - T_C}{T_H} \tag{5}$$

Here, η_{car} is the ideal cycle with the maximum thermal efficiency, T_H is the temperature of the hot source, and T_C is the temperature of the cold source.

2.3. Selection of the Working Fluid

ORCs can employ various organic refrigerants as working fluids, and the selection of the working fluid is crucial, as it affects the performance of the ORC. Therefore, studies have been conducted on various organic refrigerants. Hettiarachchi et al. [28] investigated the exergy efficiency of the ORC for various working fluids, such as ammonia, HCFC-123, n-pentane, and PF5050. In their study, the ammonia cycle efficiency was significantly lower than that of the other working fluids. Dai et al. [29] analyzed the ORC efficiency by considering 10 different working fluids under the same given waste heat condition. The results showed that the exergy efficiency of the cycles with organic working fluids was significantly better than that of the cycles using water. The exergy efficiency of the cycle using R236EA was highest at 13.26%. Yamamoto et al. [30] performed a numerical simulation and experiments to investigate the effect of working fluids (HCFC-123 and water) on the ORC performance. According to the numerical analysis results, HCFC-123 exhibited higher turbine output than water. In addition, experimental results showed that HCFC-123 significantly improved the cycle performance. In the present study, R245fa (HFC-245fa) was selected as the working fluid to recover industrial waste heat at approximately 100 °C. It is an eco-friendly organic refrigerant [31] and is suitable for the recovery of low-temperature heat sources, as its boiling point is 15.25 °C under atmospheric pressure. Table 3 lists the thermodynamic properties of R245fa.

Table 3. Properties of working fluid R245fa [31].

Molecular Mass	Critical Temperature	Critical Pressure	Evaporation Temperature (at 1 atm)	ODP	GWP
134.05 g/mol	154.01 °C	36.51 bar	15.25 °C	0	1030

3. Mean-Line Design of the Turbine

3.1. Description of the Mean-Line Design

Preliminary design is an essential step in the development of a 3D blade. In the present study, the preliminary design of the two-stage axial turbine was performed based on 1D mean-line flow modeling. Mean-line flow modeling assumes a vortex-free and uniform flow at the mid-span of the blade and provides us with various parameters such as size, rotational speed, velocity triangle, efficiency, and power of the turbine. Therefore, the mean-line flow modeling methodology has been used for the design of various turbine blades. Jubori et al. [13,14] used mean-line flow modeling in the development of innovative axial- and radial-flow turbines and considered velocity triangle and dimensionless parameters as key factors in the design process. Tournier and El-Genk [32] designed a multistage axial-flow turbine and compressor using mean-line through-flow analysis. They described

the detailed calculation procedure of the thermodynamic properties at the blade cascade inlet and outlet, as well as the pressure loss coefficient in the blades. Sim et al. [25] designed a 20 kW axial turbine based on mean-line flow modeling and used the generalized reduced gradient (GRG) nonlinear algorithm to induce the minimum total pressure loss coefficient through the mean-line design process.

3.2. Design Parameters and Velocity Triangle

The key parameters in the turbine design are the flow coefficient, Φ; loading (work) coefficient, Ψ; and degree of reaction, Z. Each parameter is a dimensionless number and is calculated as follows:

$$\Phi = \frac{V_x}{U} = \frac{V_x}{r_m\omega}, \quad \Psi = \frac{\Delta h_{stage}}{U^2} = \frac{\dot{W}_t/(N_{stage}\dot{m})}{(r_m\omega)^2}$$
$$Z = \frac{\Delta T_{rotor}}{\Delta T_{stage}} = \frac{\Delta P_{rotor}}{\Delta P_{stage}} \tag{6}$$

In these equations, U is the blade velocity, r_m is the blade mean radius, ω is the angular velocity, V_x is the meridional velocity, h is the enthalpy, and N_{stage} is the number of turbine stages. Therefore, Φ and Ψ can directly affect the turbine mass flow rate and turbine power, respectively. Z indicates the temperature (or pressure) difference in the rotor with respect to the temperature (or pressure) difference in the stage, and it may affect the expansion of the stator and rotor. If Z is small, the acceleration of the working fluid can be increased because of an increase in the expansion at the nozzle [33].

Figure 3 shows the blade and velocity components of the two-stage axial turbine. The single-stage turbine consists of a pair of stator and rotor cascades, and the two-stage turbine has the first and second stages arranged in sequence. The leading edge refers to the foremost edge of the blade, and the trailing edge—to the rearmost edge of the blade. The chord, C, is the straight-line distance between the leading and trailing edges. The axial chord, C_x, is the distance between the leading and trailing edges in the meridional plane. The pitch, S, is the straight-line distance between the adjacent blades' leading edges in the blade cascade. The velocity triangle is an index that represents the velocity and direction of the working fluid at the turbine cascade inlet and outlet, and it is calculated using dimensionless numbers (Φ, Ψ, and Z) as follows [33,34]:

$$V_2 = \frac{V_x}{cos\alpha_2}, \quad W_2 = \frac{V_x}{cos\beta_2}$$
$$tan\alpha_2 = tan\beta_2 + \frac{1}{\Phi}, \quad tan\beta_2 = \frac{\Psi/2-Z}{\Phi} \tag{7}$$

$$V_3 = \frac{V_x}{cos\alpha_3}, \quad W_3 = \frac{V_x}{cos\beta_3}$$
$$tan\alpha_3 = tan\beta_3 - \frac{1}{\Phi}, \quad tan\beta_3 = \frac{\Psi/2+Z}{\Phi} \tag{8}$$
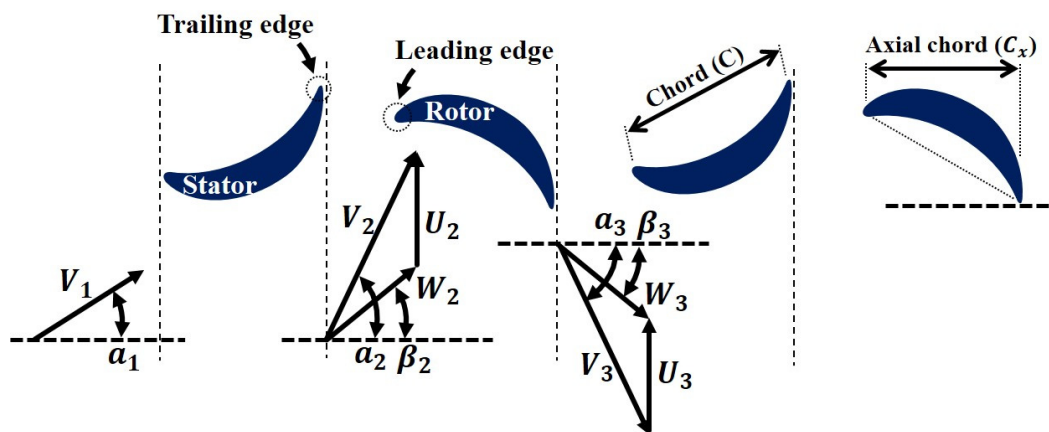

Figure 3. Cross-sectional blade shape of the two-stage axial turbine and velocity triangle.

Here, V is the absolute velocity of the working fluid, W is the relative velocity of the working fluid with respect to rotor rotation, and α and β are the angles between the meridional plane and V and W, respectively. In Figure 3, V_1 is the absolute velocity of the working fluid introduced into the first-stage stator, which is determined by the turbine mass flow rate. The angle α_1 was set to $0°$.

The specific speed of the turbine, N_s, is used for predicting the efficiency of the turbine in the Balje diagram [35] and is defined as a dimensionless number as follows [36]:

$$N_s = \frac{\Omega Q^{1/2}}{\Delta H_s^{3/4}} \tag{9}$$

Here, Q is the volume flow based on the exit conditions, ΔH_s is the isentropic specific work based on the total pressure ratio, and Ω is the rotational speed of the turbine rotor. Therefore, in the mean-line design process, the value of N_s varies depending on the thermodynamic properties of the working fluid at the turbine blade inlet and outlet as well as Ω, and a unique N_s value is derived according to the stage. According to Dixon and Hall [37], the axial turbine reaches maximum efficiency in the N_s range from 0.3 to 1.5.

3.3. Loss Models

When the working fluid passes through the turbine blades, irreversible processes cause pressure loss, which increases entropy and decreases the efficiency of the turbine. The total pressure loss explains the direct loss of the total pressure when the working fluid passes through the turbine cascade. The total pressure loss coefficient, Y, includes various loss coefficients, such as profile, secondary flow, blade tip clearance, trailing edge, supersonic expansion, shock, and lashing wire [38]. In the present study, four loss coefficients were considered in the calculation of Y in the mean-line design process. In particular, the loss calculation formula suggested by Kacker and Okapuu [39] was used. In turn, this formula is based on the loss models of Ainley and Mathieson [40] and Dunham and Came [41] (AMDC):

$$Y = Y_p + Y_s + Y_{TC} + Y_{TET} \tag{10}$$

The profile loss coefficient, Y_p, represents the loss generated at the turbine blade surface and is calculated as follows [39–41]:

$$Y_P = 0.914 \left(\frac{2}{3} Y_{P,AMDC} K_P + Y_{shock} \right) f(Re) \tag{11}$$

$$f(Re) = \left(\frac{Re}{2 \times 10^5} \right)^{-0.4} \quad \text{for } Re \leq 2 \times 10^5 \tag{12}$$

The secondary flow loss coefficient, Y_s, is generated as the flow turns in the turbine blade passage [30]. It is calculated as follows [39–41]:

$$Y_s = 1.2(Y_{S,AMDC} K_s) \tag{13}$$

$$K_s = 1 - K_3(1 - K_P) \tag{14}$$

The tip clearance loss coefficient, Y_{TC}, represents the loss that occurs in the gap between the turbine and the casing. The loss increases with the gap. Y_{TC} is calculated as follows [40,41]:

$$Y_{TC} = B \frac{c}{h} \left(\frac{k}{c} \right)^{0.78} \left(\frac{C_L}{s/c} \right)^2 \frac{cos^2 a_2}{cos^3 a_m} \quad \text{for B} = 0.37 \text{(shrouded)} \tag{15}$$

$$k = \text{(geometrical gap height)} \times \text{(number of seals)}^{-0.42} \tag{16}$$

The trailing edge loss coefficient, Y_{TET}, represents the loss caused by the influence of the turbine trailing edge thickness on the flow path. The loss increases with the trailing edge thickness. Y_{TET} is calculated as follows [38,42]:

$$Y_{TET} = \frac{2\Delta P_t}{\rho W_2^2} = \left[\frac{t_2}{s\,sin\beta_g - t_2} \right]^2 \tag{17}$$

$$\Delta P_t = \frac{1}{2}\rho W_2^2 \left[\frac{s\,sin\beta_g}{\left(s\,sin\beta_g - t_2 \right) - 1} \right]^2 \tag{18}$$

4. Flowchart of Turbine Design

Figure 4 depicts a flowchart that illustrates the turbine mean-line design and numerical analysis performed herein. The turbine inlet temperature and pressure, as well as the turbine power, $\dot{W}_t$, were selected based on the ORC operating conditions listed in Table 2, whereas the rotational speed of the rotor, Ω, was fixed at 12,000 rpm. The turbine mean radius, r_m, and velocity triangle were then calculated by selecting the initial values of the mass flow rate, flow coefficient, loading coefficient, and degree of reaction. In addition, to increase the efficiency of the turbine, design parameters that minimized the total pressure loss coefficient, Y, such as chord, axial chord, and pitch, were selected. To this end, an in-house code, introduced in a previous study [25], that includes the GRG nonlinear algorithm was applied in the mean-line design process. The code determines design parameters that minimize the Y value based on the aspect ratio, solidity, and Zweifel blade loading coefficient. In the present study, the aspect ratio ranged from 1.0 to 2.0 [43], the solidity from 1.2 to 1.8 [44], and the Zweifel blade loading coefficient from 1.0 to 2.0 [45]. The solution was obtained by numerical differentiation based on the centered divided difference scheme, and a tolerance of 10^{-3} was selected as the convergence criterion. The GRG nonlinear algorithm is significantly affected by the initial values, and the calculation most likely will stop at a region other than the global optimum solution. However, the algorithm is a powerful tool in the turbine mean-line design because it can rapidly identify a local optimum solution near the initial conditions. The reliability of the GRG nonlinear algorithm applied to the in-house code was verified because it used commercial code provided by Microsoft Excel 2016.

The specific speed, N_s, varied based on the mass flow rate when the turbine inlet conditions, $\dot{W}_t$, and Ω, were constant. The mass flow rate was adjusted within the range that satisfied the recommended range of N_s from 0.3 to 1.5 [37]. Three-dimensional blade modeling was performed based on the 1D blade geometric parameters selected as optimal values through the in-house code. In the present study, SoftInWay AxSTREAM (version 3.9.12) was used to perform 3D blade modeling. In addition, Siemens Simcenter STAR-CCM+ (version 2019.1) was used for numerical analysis of the completed turbine 3D blade geometry. Finally, the performance of the turbine was evaluated using the numerical analysis results for the 3D turbine blade.
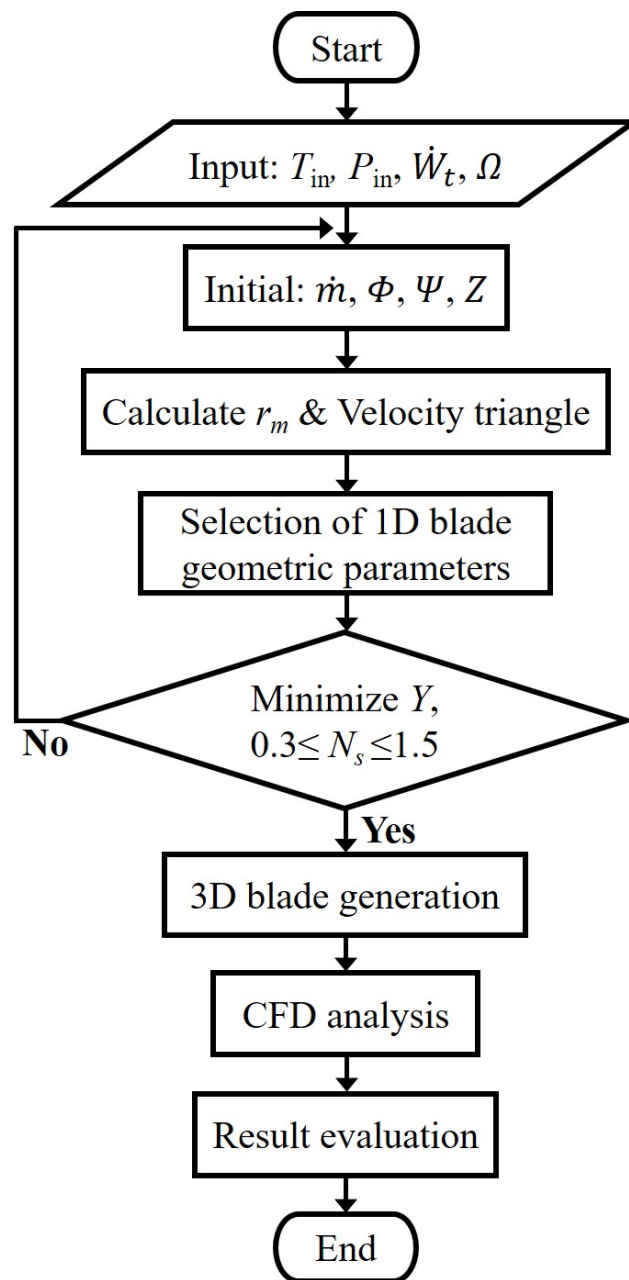
```
                    ┌───────────┐
                    │   Start   │
                    └───────────┘
                          │
                          ▼
          ╱─────────────────────────────────╲
          │  Input: T_in, P_in, Ẇ_t, Ω      │
          ╲─────────────────────────────────╱
                          │
                          ▼
              ┌───────────────────────┐
              │  Initial: ṁ, Φ, Ψ, Z  │
              └───────────────────────┘
                          │
                          ▼
          ┌─────────────────────────────┐
          │ Calculate r_m & Velocity    │
          │            triangle         │
          └─────────────────────────────┘
                          │
                          ▼
          ┌─────────────────────────────┐
          │   Selection of 1D blade     │
          │    geometric parameters     │
          └─────────────────────────────┘
                          │
                          ▼
              ╱───────────────────────╲
              │     Minimize Y,        │
       No ◄───│   0.3 ≤ N_s ≤ 1.5      │
              ╲───────────────────────╱
                          │ Yes
                          ▼
              ┌───────────────────────┐
              │   3D blade generation │
              └───────────────────────┘
                          │
                          ▼
              ┌───────────────────────┐
              │     CFD analysis      │
              └───────────────────────┘
                          │
                          ▼
              ┌───────────────────────┐
              │   Result evaluation   │
              └───────────────────────┘
                          │
                          ▼
                    ┌───────────┐
                    │    End    │
                    └───────────┘
```

Figure 4. Flowchart of the turbine mean-line design and numerical analysis.

5. Numerical Analysis Procedures

In the turbine mean-line design, the turbine efficiency can be calculated by evaluating the thermodynamic state and velocity of the working fluid at the turbine inlet and outlet. Because the turbine blade has a 3D geometry, the turbine performance cannot be accurately predicted through the 1D mean-line design. Therefore, in the present study, the 3D blade geometry was modelled in detail based on the mean-line design, and numerical analysis was conducted to predict the performance of the turbine more accurately. First, SoftInWay AxSTREAM (version 3.9.12) was used to convert the 1D mean-line design results into 3D. In the 3D design of the turbine blade, the thickness, gap, and angle of the blades were modified in detail according to the spanwise direction. Figure 5 shows the 3D-modeled blade geometry of the two-stage axial turbine. For the designed 3D blade, a twist was applied in the spanwise direction, and the rotor rotated in the counterclockwise direction. The height of the blade was gradually increased in the axial direction for the expansion

of the working fluid. In this instance, the blade mean radius remained constant. As shown in Figure 5, a pair of blades was used as a domain for the numerical analysis in the present study. This is because the analysis time was shorter than in the full-scale domain that included all blades. The analysis reliability could be improved by constructing a denser grid.

Figure 5. Three-dimensional blade geometry of the two-stage axial turbine.

Siemens Simcenter STAR-CCM+ (version 2019.1) was used in the present study to conduct numerical analysis on the designed 3D turbine blade geometry. Numerical analysis included meshing, solution, and post-processing procedures. First, a grid was generated around the turbine blade, as shown in Figure 6. As the intensity of the turbulence is high around the turbine blade, a grid should be constructed close to the blade boundary layer. Therefore, in the present study, the dimensionless wall distance, y^+, was set to 1 or lower. A small y^+ value indicates that the distance from the blade wall to the center of the closest grid decreases. A complicated turbulence flow requires a very fine grid near the blade wall, so that $y^+ < 1$ [46,47]. However, if all grids around the blade are dense, the number of grids becomes large, increasing the analysis time. Therefore, as shown in Figure 6, grids were generated so that their density gradually decreased with increasing distance from the blade boundary layer. In the present study, a total of 750,000 grids were generated based on a pair of blades.

In the turbine simulation, the flow was assumed 3D, compressible, steady-state, and viscous. The working fluid was R245fa, and its properties were obtained from the National Institute of Standards and Technology (NIST) REFPROP database (version 10.0) and were applied to the software using the real gas equation of the state model. In addition, a stagnation inlet condition was set for the inlet, and a static pressure outlet condition for the outlet. A no-slip adiabatic condition was set for the blade wall. For the complex flow analysis around the blade, the shear stress transport (SST) k–ω turbulent model, based on the Reynolds-averaged Navier–Stokes (RANS), model was selected [48,49]. This model is based on a two-equation eddy-viscosity model, which is a combination of the Wilcox [50] k–ω model near the wall and the k–ε model at a remote boundary [51,52]. The convergence criterion of the simulation was decided considering that the root mean square

error decreased under a value of 10^{-3}. The equations of the SST k–ω turbulent model are as follows:

$$\frac{D\rho k}{Dt} = \tau_{ij}\frac{\partial u_i}{\partial x_j} - \rho\beta k\omega + \frac{\partial}{\partial x_j}\left[\left(\mu + \frac{\mu_t}{\sigma_k}\right)\frac{\partial k}{\partial x_j}\right] \tag{19}$$

$$\frac{D\rho\omega}{Dt} = \frac{\gamma}{\nu_t}\tau_{ij}\frac{\partial u_i}{\partial x_j} - \rho\beta\omega^2 + \frac{\partial}{\partial x_j}\left[\left(\mu + \frac{\mu_t}{\sigma_\omega}\right)\frac{\partial \omega}{\partial x_j}\right] + 2\rho(1-F_1)\sigma_{\omega 2}\frac{1}{\omega}\frac{\partial k}{\partial x_j}\frac{\partial \omega}{\partial x_j} \tag{20}$$

Here, k is the turbulent kinetic energy, μ_t is the turbulent viscosity, and ω is the turbulent energy dissipation rate. The Reynolds stress tensor, τ_{ij}, is expressed using Boussinesq's eddy-viscosity concept as follows:

$$\tau_{ij} = 2\mu_t S_{ij} - \frac{2}{3}\rho k\delta_{ij} \tag{21}$$

Here, S_{ij} is the time-average strain rate tensor, and δ_{ij} is the Kronecker delta.
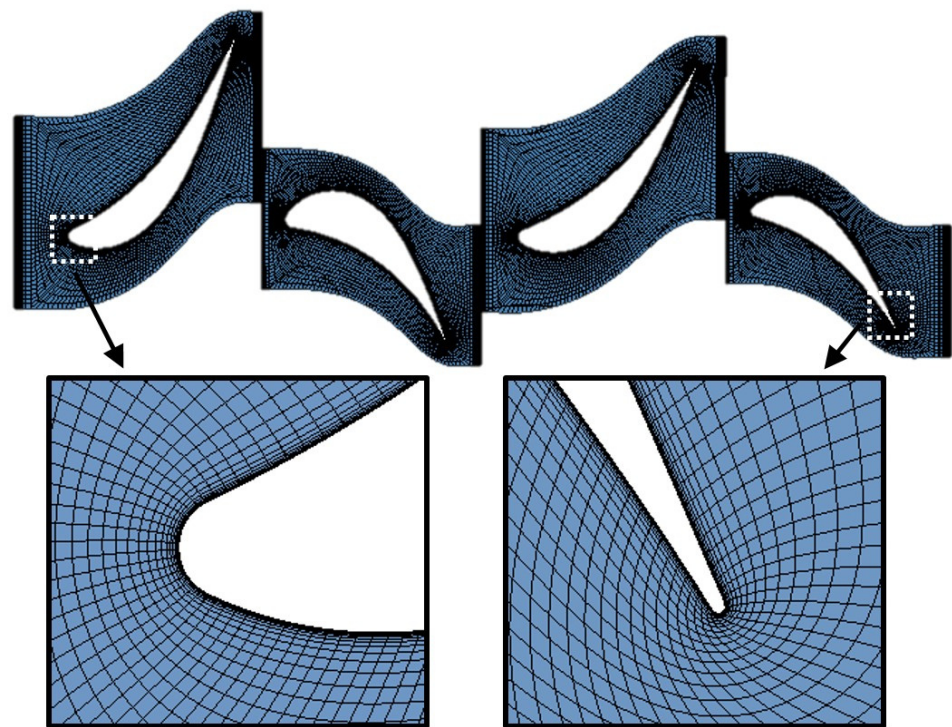
Figure 6. Construction of a grid around the turbine blades for numerical analysis.

6. Results and Discussion

6.1. Validation

The mean-line design procedure performed in the present study was verified through a previous study [25]. In the experimental model for the verification, the two-stage turbine geometry and experimental results presented by Kofskey and Nusbaum [53] were used. Figure 7 shows the turbine total-to-static isentropic efficiency, η_t, for the flow coefficient. The experiment results [53] were compared with the 1D mean-line design results. The tendencies in the graphs of the two cases showed good agreement with insignificant errors. When the flow coefficient was 0.61, η_t was approximately 79% for the experimental results and 76% for the mean-line design results. The errors arose due to the difference in the turbine blade dimensions; thus, the obtained errors are reasonable.
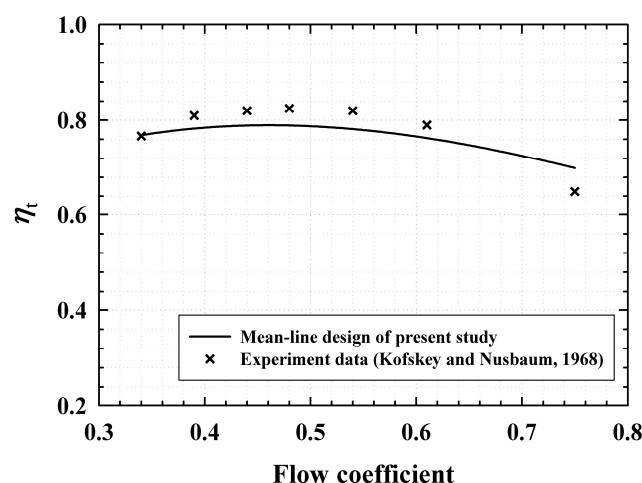
Figure 7. Turbine efficiency comparison between the mean-line design results and the experimental results [53].

6.2. Mean-Line Design

Table 4 shows the main parameters and corresponding results of the mean-line-designed two-stage axial turbine rotor. The blade mean radius was 70.89 mm, and this value was applied to the stator and rotor of each stage in the same manner. In addition, the tip clearance height of the rotor was designed to be 0.5 mm. The turbine efficiency could be increased by decreasing this value, but the manufacturing limitation of the range was considered. In the present study, for the design of a 180 kW axial turbine, the loading coefficient, Ψ, was set to 1.18. According to Equation (6), the rotational speed of the two-stage axial turbine at constant Ψ is 12,000 rpm, but the rotational speed is approximately 17,000 rpm when the single-stage is applied. A two-stage turbine was implemented in the present study because of the reduction in rotational speed, as compared with that of a single-stage turbine. Consequently, the results presented in Table 4 were used as the basis for the 3D turbine design.

Table 4. Mean-line design results for the two-stage axial turbine rotor.

Design Parameters	Value		
	First-Stage		Second-Stage
Flow coefficient, Φ		0.27	
Loading coefficient, Ψ		1.18	
Degree of reaction, Z		0.50	
Blade mean radius, r_m [mm]		70.89	
Number of blades	59		63
Axial chord, C_x [mm]	9.23		8.13
Chord, C [mm]	11.28		10.57
Pitch, S [mm]	7.92		7.41
Zweifel blade loading coefficient	1.03		1.00
Tip clearance height [mm]		0.50	
Trailing edge thickness [mm]	0.142		0.135

Figure 8 shows the turbine blade mean radius, r_m, for the turbine mass flow rate, $\dot{m}$. Equation (6) was used to calculate r_m. In this instance, the turbine power, $\dot{W}_t$, was 180 kW, and the rotational speed, Ω, was 12,000 rpm. Consequently, under a constant-Ψ condition, r_m gradually decreased as $\dot{m}$ was gradually increased. This was because of the difference in total enthalpy: Δh decreased, and thus r_m also decreased if $\dot{W}_t$ was fixed and $\dot{m}$ was increased according to Equation (6). In the present study, $\dot{m}$ was 9.61 kg/s at the design point, and in this instance, r_m was 70.89 mm. These results were obtained for the

two-stage turbine. For the single-stage turbine under the same turbine output conditions, r_m increased.
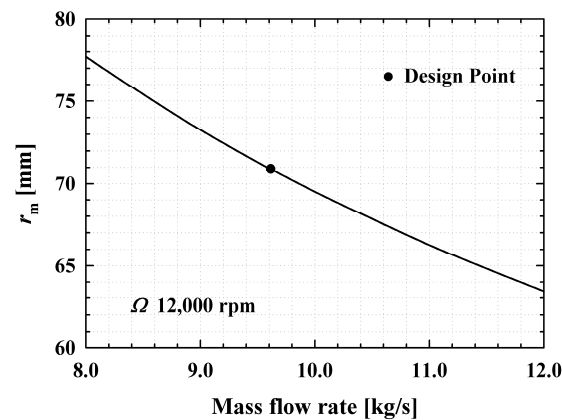

Figure 8. Turbine blade mean radius versus mass flow rate at a rotational speed of 12,000 rpm.

The specific speed of the turbine, N_s, could be calculated using Equation (9). In Figure 9, N_s was calculated according to $\dot{m}$ when Ω was 12,000 rpm and $\dot{W}_t$ was 180 kW based on the single-stage. As $\dot{m}$ increased, N_s increased. At the design point ($\dot{m} = 9.61$ kg/s), N_s was 0.83 for the first-stage turbine and 1.07 for the second-stage turbine. The N_s of the first-stage turbine was lower than that of the second-stage turbine because of the density of the working fluid, which was affected by the temperature and pressure at the corresponding points. The density at the turbine first-stage outlet was higher than that at the second-stage outlet. Consequently, if Ω and $\dot{W}_t$ were constant, N_s also increased with $\dot{m}$. As the flow rate was increased to 11.2 kg/s or higher, second-stage N_s exceeded 1.2. Because $\dot{m}$ directly affected N_s in the turbine mean-line design procedure, an appropriate flow rate had to be selected to obtain results that satisfied the recommended range from 0.3 to 1.5 [37].
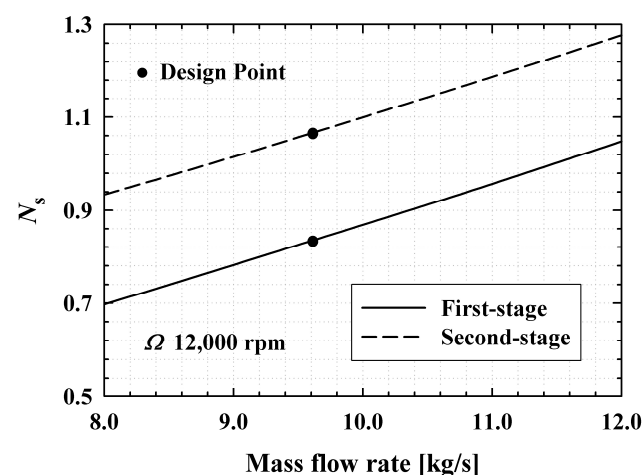
Figure 9. Turbine specific speed versus mass flow rate at a rotational speed of 12,000 rpm.

6.3. Numerical Analysis

The state of the working fluid passing through the turbine and the performance of the turbine were predicted by conducting numerical analysis on the designed 3D turbine geometry. Figure 10 shows the temperature of the working fluid passing through the turbine blades. The turbine inlet temperature is approximately 85 °C, and the temperature gradually decreases as the fluid passes through the turbine blades. This phenomenon occurs as the thermal energy received from the heat source is converted into mechanical energy during the turbine operation, and the temperature decrement increases as the work

performed by the turbine increases. In the case of the turbine designed in the present study, the temperature decreased by approximately 35 °C while the working fluid passed through the turbine. Figure 11 shows the pressure of the working fluid passing through the turbine blade. Similar to the temperature trend, the pressure of the working fluid passing through the turbine blade gradually decreased. Based on the turbine inlet total pressure of 0.75 MPa, the total-to-static pressure ratio of the designed turbine was 3.0, and thus the pressure of the working fluid passing through the second-stage rotor was approximately 0.25 MPa.
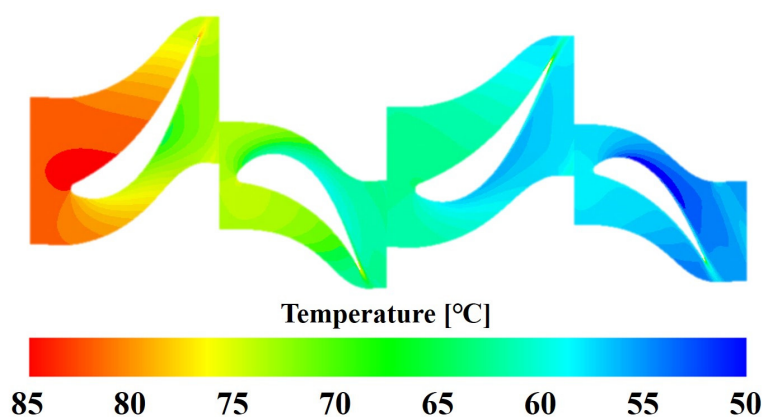
Figure 10. Temperature distribution at the mid-span of the two-stage axial turbine blade.
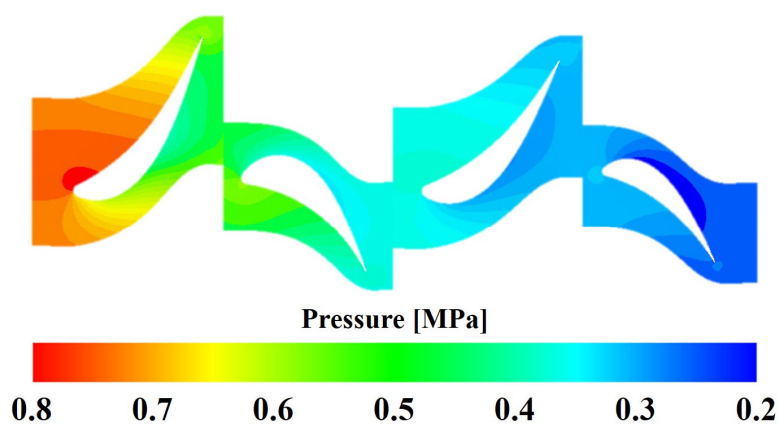
Figure 11. Pressure distribution at the mid-span of the two-stage axial turbine blade.

Figure 12 shows the turbine total-to-static isentropic efficiency, η_t, with respect to the number of grids for the numerical analysis on the designed 3D turbine. Here, η_t was calculated based on the turbine inlet total pressure and turbine outlet static pressure. Consequently, as the number of grids gradually increased, the reliability of the analysis improved, simultaneously increasing η_t. When the number of grids reached approximately 680,000, η_t converged to some value and remained constant. Therefore, in the present study, 750,000 grids were used for predicting the performance of the designed turbine.

Furthermore, η_t predicted using numerical analysis was compared with the mean-line design result presented in Figure 13. When η_t is examined based on the turbine total-to-static pressure ratio, *PR*, the two efficiency curves have similar trends, and the peak η_t occurs near *PR* 3.0 in both cases. Based on the turbine design point (Ω 12,000 rpm and *PR* 3.0), η_t predicted using the mean-line design is 86.7%, which is slightly higher than the numerical analysis result. This is because the numerical analysis uses the 3D turbine blade and, thus, reflects more losses than the 1D mean-line design.
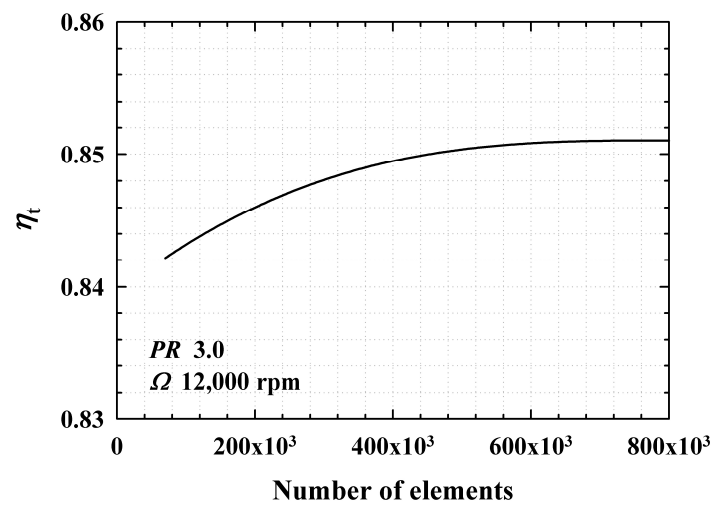
Figure 12. Turbine total-to-static efficiency versus number of grids around the blade.
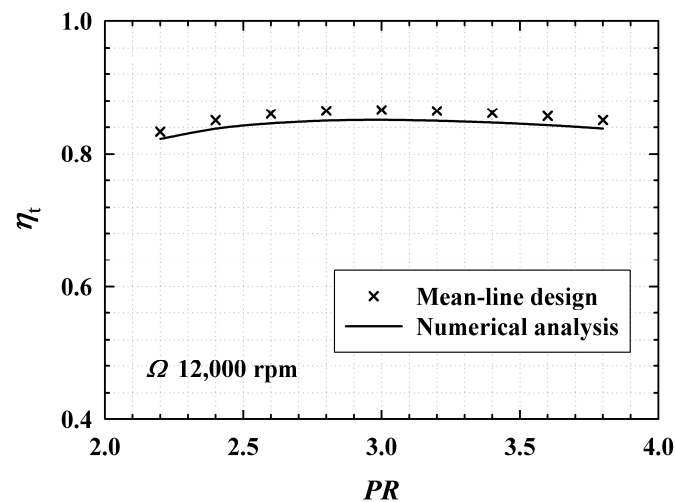

Figure 13. Turbine total-to-static efficiency comparison between the numerical analysis results and the mean-line design results.

The off-design analysis of η_t was conducted according to the rotational speed, Ω, and *PR*, using numerical analysis. The results are presented in Figure 14. A unique peak η_t appears for each Ω, and peak η_t appears at higher *PR* with increasing Ω. When the turbine *PR* increases to 3.2 or higher, η_t is higher with increasing turbine Ω. Consequently, η_t predicted at the turbine design point (Ω = 12,000 rpm and *PR* = 3.0) is 85.1%, and η_t is predicted to be 84.8% and 82.7% when the Ω value is 13,200 rpm and 9600 rpm, respectively. In Figure 15, the turbine power, $\dot{W}_t$, is predicted according to the turbine *PR* and Ω. Regardless of the turbine Ω, $\dot{W}_t$ increases with *PR*. This is because the turbine mass flow rate, $\dot{m}$, increases with *PR*. If $\dot{m}$ is increased, $\dot{W}_t$ also increases according to Equation (1). When the turbine *PR* is increased to 3.2 or higher, $\dot{W}_t$ increases with increasing turbine Ω. This trend coincides with that of η_t in Figure 13. Based on the turbine Ω of 12,000 rpm, $\dot{W}_t$ increases to approximately 217 kW when the *PR* is increased to 4.0. Therefore, $\dot{W}_t$ can be increased by increasing the turbine *PR*. For a fixed turbine geometry, however, the *PR* can be increased only within a limited range. Consequently, for the designed turbine, $\dot{W}_t$ is predicted to be 176.1 kW at the design point (Ω = 12,000 rpm and *PR* = 3.0).
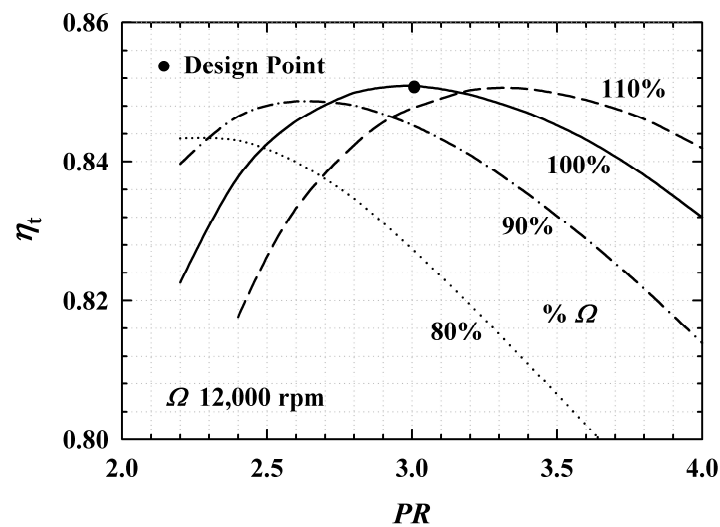
Figure 14. Turbine total-to-static efficiency versus pressure ratio for various rotational velocities.
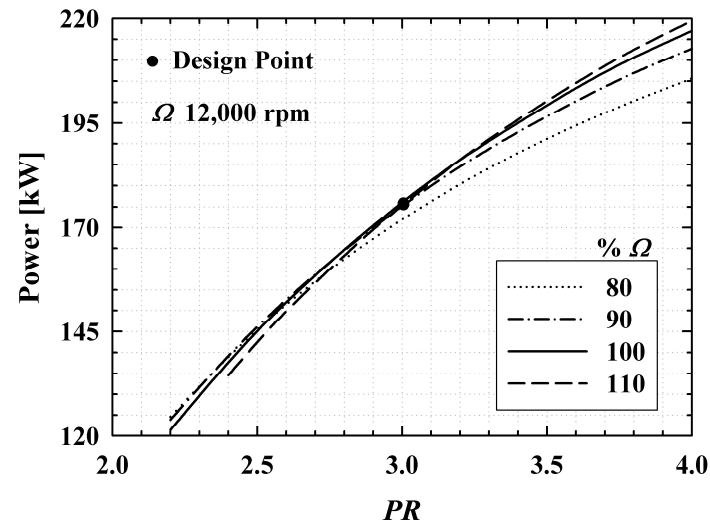
Figure 15. Turbine power versus pressure ratio for various rotational velocities.

6.4. ORC Thermal Efficiency

The working condition parameters selected in Table 2 were used for the ORC system design. In this instance, the numerical analysis results were used for the efficiency and output of the turbine. As shown in Figure 16, the thermal efficiency and exergy efficiency of ORC are predicted to be 7.40% and 34.49%, respectively. In this instance, the temperature of the working fluid at the condenser outlet is assumed to be 25 °C considering the heat exchange from the cold source. In addition, the heat transfer capacity of the evaporator is designed to be 2.26 MW, and that of the condenser is 2.11 MW. When the pump efficiency is 75%, the power consumption of the pump is 5.03 kW. Considering a generator efficiency of 98%, the net power of the ORC system is 167.5 kW. In this instance, the mechanical efficiency of the ORC system is neglected. The thermal efficiency of the ORC can be increased by minimizing the supercooling of the working fluid in the condenser. When the temperature of the working fluid at the condenser outlet is assumed to be 35 °C, the thermal efficiency and exergy efficiency of the ORC are improved to 7.83% and 36.54%, respectively.
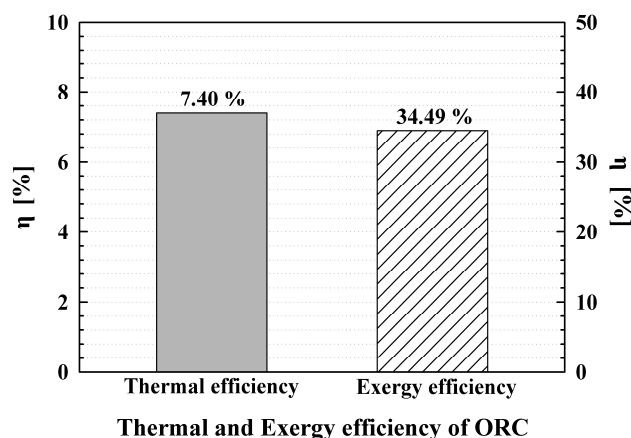
Figure 16. Thermal efficiency and exergy efficiency of the ORC.

7. Conclusions

The design of the turbine that converts thermal energy into electrical energy is specifically important among the other components of the ORC. In the present study, a 180 kW two-stage axial turbine yielding high-efficiency even at a low rotational speed (12,000 rpm) was designed. If the rotational speed of the turbine is decreased, ball bearings can be used, thereby reducing the turbine system manufacturing cost. Herein, to design a high-efficiency turbine, design parameters that minimized the total pressure loss coefficient were determined using an in-house code that included the GRG nonlinear algorithm in the mean-line design process. Based on the results of 3D numerical analysis, the total-to-static isentropic efficiency and electrical power of the designed turbine were predicted to be 85.1% and 176.1 kW, respectively. Furthermore, an ORC was designed, and its performance was predicted using the numerical analysis-based turbine performance results. When the condenser outlet temperature was assumed to be 25 °C, the thermal efficiency and exergy efficiency of the ORC were 7.40% and 34.49%, respectively. This study implies the applicability of various rotational speed and number of stages for an axial turbine in the ORC. In the future, the performance of the two-stage axial turbine will be verified via an air similarity test.

Author Contributions: Conceptualization, J.-B.S. and Y.W.K.; methodology, J.-B.S. and Y.W.K.; software, J.-B.S. and S.-J.Y.; validation, J.-B.S. and S.-J.Y.; formal analysis, J.-B.S.; investigation, J.-B.S.; resources, J.-B.S.; data curation, J.-B.S. and S.-J.Y.; writing—original draft preparation, J.-B.S.; writing—review and editing, J.-B.S. and Y.W.K.; visualization, J.-B.S.; supervision, Y.W.K.; project administration, J.-B.S. and Y.W.K.; funding acquisition, Y.W.K. All authors have read and agreed to the published version of the manuscript.

Data Availability Statement: Not applicable.

Conflicts of Interest: The authors declare no conflict of interest.

References

1. Loni, R.; Najafi, G.; Bellos, E.; Rajaee, F.; Said, Z.; Mazlan, M. A Review of Industrial Waste Heat Recovery System for Power Generation with Organic Rankine Cycle: Recent Challenges and Future Outlook. *J. Clean. Prod.* **2021**, *287*, 125070. [CrossRef]
2. Cataldo, F.; Mastrullo, R.; Mauro, A.W.; Vanoli, G.P. Fluid Selection of Organic Rankine Cycle for Low-Temperature Waste Heat Recovery Based on Thermal Optimization. *Energy* **2014**, *72*, 159–167. [CrossRef]

3. Tchanche, B.F.; Lambrinos, G.; Frangoudakis, A.; Papadakis, G. Low-Grade Heat Conversion into Power Using Organic Rankine Cycles–A Review of Various Applications. *Renew. Sustain. Energy Rev.* **2011**, *15*, 3963–3979. [CrossRef]

4. Quoilin, S.; Van Den Broek, M.V.D.; Declaye, S.; Dewallef, P.; Lemort, V. Techno-Economic Survey of Organic Rankine Cycle (ORC) Systems. *Renew. Sustain. Energy Rev.* **2013**, *22*, 168–186. [CrossRef]

5. Li, M.; Wang, J.; He, W.; Gao, L.; Wang, B.; Ma, S.; Dai, Y. Construction and Preliminary Test of a Low-Temperature Regenerative Organic Rankine Cycle (ORC) Using R123. *Renew. Energy* **2013**, *57*, 216–222. [CrossRef]

6. Peng, N.; Wang, E.; Zhang, H. Preliminary Design of an Axial-Flow Turbine for Small-Scale Supercritical Organic Rankine Cycle. *Energies* **2021**, *14*, 5277. [CrossRef]

7. Fu, B.R.; Lee, Y.R.; Hsieh, J.C. Design, Construction, and Preliminary Results of a 250-kW Organic Rankine Cycle System. *Appl. Therm. Eng.* **2015**, *80*, 339–346. [CrossRef]

8. Pei, G.; Li, J.; Li, Y.; Wang, D.; Ji, J. Construction and Dynamic Test of a Small-Scale Organic Rankine Cycle. *Energy* **2011**, *36*, 3215–3223. [CrossRef]

9. Kang, S.H. Design and Experimental Study of ORC (Organic Rankine Cycle) and Radial Turbine Using R245fa Working Fluid. *Energy* **2012**, *41*, 514–524. [CrossRef]

10. Klonowicz, P.; Borsukiewicz-Gozdur, A.; Hanausek, P.; Kryłłowicz, W.; Brüggemann, D. Design and Performance Measurements of an Organic Vapour Turbine. *Appl. Therm. Eng.* **2014**, *63*, 297–303. [CrossRef]

11. Giovannelli, A.; Archilei, E.M.; Salvini, C. Two-Stage Radial Turbine for a Small Waste Heat Recovery Organic Rankine Cycle (ORC) Plant. *Energies* **2020**, *13*, 1054. [CrossRef]

12. Li, M.; Wang, J.; Gao, L.; Niu, X.; Dai, Y. Performance Evaluation of a Turbine Used in a Regenerative Organic Rankine Cycle. In Turbo Expo: Power for Land, Sea, and Air. *Am. Soc. Mech. Eng.* **2012**, *44724*, 425–432.

13. Al Jubori, A.M.; Al-Dadah, R.; Mahmoud, S. An Innovative Small-Scale Two-Stage Axial Turbine for Low-Temperature Organic Rankine Cycle. *Energy Convers. Manag.* **2017**, *144*, 18–33. [CrossRef]

14. Al Jubori, A.; Daabo, A.; Al-Dadah, R.K.; Mahmoud, S.; Ennil, A.B. Development of Micro-scale Axial and Radial Turbines for Low-Temperature Heat Source Driven Organic Rankine Cycle. *Energy Convers. Manag.* **2016**, *130*, 141–155. [CrossRef]

15. Breńkacz, Ł.; Żywica, G.; Bogulicz, M. Selection of the Oil-Free Bearing System for a 30 kW ORC Microturbine. *J. Vibroeng.* **2019**, *21*, 318–330. [CrossRef]

16. Breńkacz, Ł.; Żywica, G.; Bogulicz, M. Selection of the Bearing System for a 1 kW ORC Microturbine. In Proceedings of the International Conference on Rotor Dynamics, Rio de Janeiro, Brazil, 23–27 September 2018; Springer: Cham, Switzerland, 2018; pp. 223–235.

17. Dhanola, A.; Garg, H.C. Tribological challenges and advancements in wind turbine bearings: A review. *Eng. Fail. Anal.* **2020**, *118*, 104885. [CrossRef]

18. Lim, H.S.; Choi, B.S.; Park, M.R.; Hwang, S.C.; Park, J.Y.; Seo, J.; Bang, J.S.; Kim, B.O. Performance evaluation of two-stage turbine for the organic Rankine cycle system. *J. Mech. Sci. Technol.* **2017**, *31*, 5849–5855. [CrossRef]

19. Żywica, G.; Breńkacz, Ł.; Bagiński, P. Interactions in the rotor-bearings-support structure system of the multi-stage ORC microturbine. *J. Vib. Eng. Technol.* **2018**, *6*, 369–377. [CrossRef]

20. Breńkacz, Ł.; Żywica, G.; Bogulicz, M. Analysis of dynamical properties of a 700 kW turbine rotor designed to operate in an ORC installation. *Diagnostyka* **2016**, *17*, 17–23.

21. Zhao, Y.; Liu, G.; Li, L.; Yang, Q.; Tang, B.; Liu, Y. Expansion devices for organic Rankine cycle (ORC) using in low temperature heat recovery: A review. *Energy Convers. Manag.* **2019**, *199*, 111944. [CrossRef]

22. Fu, L.; Feng, Z.; Li, G. Experimental investigation on overall performance of a millimeter-scale radial turbine for micro gas turbine. *Energy* **2017**, *134*, 1–9. [CrossRef]

23. Micha, P.T.; Mohan, T.; Sivamani, S. Design and analysis of a permanent magnetic bearing for vertical axis small wind turbine. *Energy Procedia* **2017**, *117*, 291–298. [CrossRef]

24. Kozanecki, Z.; Łagodziński, J. Magnetic Thrust Bearing for the ORC High–Speed Microturbine. *Solid State Phenom.* **2013**, *198*, 348–353. [CrossRef]

25. Sim, J.B.; Yook, S.J.; Kim, Y.W. Performance Analysis of Organic Rankine Cycle with the Turbine Embedded in a Generator (TEG). *Energies* **2022**, *15*, 309. [CrossRef]

26. Walraven, D.; Laenen, B.; D'haeseleer, W. Comparison of Thermodynamic Cycles for Power Production from Low-Temperature Geothermal Heat Sources. *Energy Convers. Manag.* **2013**, *66*, 220–233. [CrossRef]

27. Baik, Y.J.; Kim, M.; Chang, K.C.; Lee, Y.S.; Yoon, H.K. A Comparative Study of Power Optimization in Low-Temperature Geothermal Heat Source Driven R125 Transcritical Cycle and HFC Organic Rankine Cycles. *Renew. Energy* **2013**, *54*, 78–84. [CrossRef]

28. Madhawa Hettiarachchi, H.D.; Golubovic, M.; Worek, W.M.; Ikegami, Y. Optimum Design Criteria for an Organic Rankine Cycle Using Low-Temperature Geothermal Heat Sources. *Energy* **2007**, *32*, 1698–1706. [CrossRef]

29. Dai, Y.; Wang, J.; Gao, L. Parametric Optimization and Comparative Study of Organic Rankine Cycle (ORC) for Low Grade Waste Heat Recovery. *Energy Convers. Manag.* **2009**, *50*, 576–582. [CrossRef]

30. Yamamoto, T.; Furuhata, T.; Arai, N.; Mori, K. Design and Testing of the Organic Rankine Cycle. *Energy* **2001**, *26*, 239–251. [CrossRef]

31. Wang, E.H.; Zhang, H.G.; Fan, B.Y.; Ouyang, M.G.; Zhao, Y.; Mu, Q.H. Study of Working Fluid Selection of Organic Rankine Cycle (ORC) for Engine Waste Heat Recovery. *Energy* **2011**, *36*, 3406–3418. [CrossRef]

32. Tournier, J.M.; El-Genk, M.S. Axial Flow, Multi-stage Turbine and Compressor Models. *Energy Convers. Manag.* **2010**, *51*, 16–29. [CrossRef]

33. Moustapha, H.; Zelesky, M.F.; Baines, N.C.; Japikse, D. *Axial and Radial Turbines*; Concepts NREC: White River Junction, VT, USA, 2003.

34. Wilson, D.G.; Korakianitis, T. *The Design of High-Efficiency Turbomachinery and Gas Turbines*; MIT Press: Cambridge, MA, USA, 2014.

35. Balje, O.E. *Turbomachines: A Guide to Design, Selection, and Theory*; Wiley Interscience: Hoboken, NJ, USA, 1981.

36. Kofskey, M.G.; Nusbaum, W.J. *Effects of Specific Speed on Experimental Performance of a Radial-Inflow Turbine*; National Aeronautics and Space Administration: Washington, DC, USA, 1972; p. E–6349.

37. Dixon, S.L.; Hall, C. *Fluid Mechanics and Thermodynamics of Turbomachinery*; Butterworth-Heinemann: Woburn, MA, USA, 2013.

38. Aungier, R.H. *Turbine Aerodynamics*; American Society of Mechanical Engineers Press: New York, NY, USA, 2006.

39. Kacker, S.C.; Okapuu, U. A Mean Line Prediction Method for Axial Flow Turbine Efficiency. *J. Eng. Power* **1982**, *104*, 111–119. [CrossRef]

40. Ainley, D.G.; Mathieson, G.C. *A Method of Performance Estimation for Axial-Flow Turbines*; Aeronautical Research Council: London, UK, 1951.

41. Dunham, J.; Came, P.M. Improvements to the Ainley-Mathieson Method of Turbine Performance Prediction. *J. Eng. Power* **1970**, *92*, 252–256. [CrossRef]

42. Benedict, R.P.; Carlucci, N.A.; Swetz, S.D. Flow Losses in Abrupt Enlargements and Contractions. *J. Eng. Power* **1966**, *88*, 73–81. [CrossRef]

43. Rist, D. Influence of geometric effects on the aspect ratio optimization of axial turbine bladings. In Proceedings of the Turbo Expo: Power for Land, Sea, and Air, ASME, London, UK, 9–13 April 1978; Volume 79726, p. V01BT02A072. [CrossRef]

44. Gao, K.; Xie, Y.; Zhang, D. Effects of rotor solidity and leakage flow on the unsteady flow in axial turbine. *Appl. Therm. Eng.* **2018**, *128*, 926–939. [CrossRef]

45. Zweifel, O. The spacing of turbomachine blading, especially with large angular deflection. *Brown Boveri Rev.* **1945**, *32*, 436–444.

46. Lanzafame, R.; Mauro, S.; Messina, M. 2D CFD Modeling of H-Darrieus Wind Turbines Using a Transition Turbulence Model. *Energy Procedia* **2014**, *45*, 131–140. [CrossRef]

47. Schramm, M.; Rahimi, H.; Stoevesandt, B.; Tangager, K. The Influence of Eroded Blades on Wind Turbine Performance Using Numerical Simulations. *Energies* **2017**, *10*, 1420. [CrossRef]

48. Menter, F.R.; Kuntz, M.; Langtry, R. Ten Years of Industrial Experience with the SST Turbulence Model. Turbulence. *Heat Mass Transf.* **2003**, *4*, 625–632.

49. Menter, F. Zonal Two Equation k-w Turbulence Models for Aerodynamic Flows. In Proceedings of the 23rd Fluid Dynamics, Plasmadynamics, and Lasers Conference, Orlando, FL, USA, 6–9 July 1993; Volume 2906. [CrossRef]

50. Wilcox, D.C. Reassessment of the Scale-Determining Equation for Advanced Turbulence Models. *AIAA J.* **1988**, *26*, 1299–1310. [CrossRef]

51. Menter, F.R. Two-Equation Eddy-Viscosity Turbulence Models for Engineering Applications. *AIAA J.* **1994**, *32*, 1598–1605. [CrossRef]

52. Wang, H.; Ding, J.; Ma, B.; Li, S. Aerodynamic Simulation of Wind Turbine Blade Airfoil with Different Turbulence Models. *J. Vibroeng.* **2014**, *16*, 2474–2483.

53. Kofskey, M.G.; Nusbaum, W.J. *Aerodynamic Evaluation of Two-Stage Axial-Flow Turbine Designed for Brayton-Cycle Space Power System*; National Aeronautics and Space Administration: Washington, DC, USA, 1968; p. D–4382.